Diffraction Model for Direct Reactions*

E. M. HENLEY AND D. U. L. YU
University of Washington, Seattle, Washington
(Received 23 April 1964)

A diffraction model for direct reactions which we proposed earlier is extended. The simple model provides physical insight into the effects of nuclear optical-model potential distortions without the necessity of performing complex numerical integrations. It is particularly useful, and can be qualitatively justified, for direct reactions when (1) strong absorption is present in both the incident and exit channels and (2) the center-of-mass wave function of the bound state involved corresponds to a small binding energy or to a long exponential tail. Thus, it is expected to be especially applicable to intermediate-energy complex-particle reactions such as the (He^3,d) and (α,t) processes. In this paper, the forward-angle approximations made earlier are removed so that time-reversal symmetry is restored. Proper bound-state wave functions outside the nucleus are employed. Coulomb effects are briefly discussed. The assumptions of the model are thus made less drastic, but at the expense of decreasing mathematical simplicity. Predictions based on the earlier version are essentially unaffected, so that the simple forward-angle model remains useful up to moderately large angles. This is illustrated by comparisons with experiments.

I. INTRODUCTION

IN a recent article[1] on double-stripping reactions, we proposed a simple (forward-angle) diffraction model for gaining some insight into distortion effects for reactions in which both incident and outgoing particles are strongly absorbed by the nucleus. This model was found to be very effective in explaining the dominant features of such processes as the (He^3,n) reaction; but it is equally valid for (α,α'), (d,p), (α,d), (α,He^3), (He^3,d), (α,Li^6) and other rearrangement or inelastic collisions in which the binding energy of the center of mass of the transferred or excited "system" is small. In particular, we were able to reproduce the forward-angle differential cross sections and the trend of the transition probability toward stronger excitation of higher angular momentum states as the difference between the momenta of the incident and emergent particle increases. Our diffraction model is also applicable for high-energy elementary-particle collisions where many competing channels are open in both initial and final states.[2] Most of our discussions, however, will be restricted to intermediate-energy direct nuclear reactions.

The diffraction model described in HY[1] involves several assumptions that might seem to make its validity questionable. For instance, the forward-angle approximation breaks time-reversal invariance and limits the applicability of the model to small scattering angles.

In this paper, we remove most of the assumptions made in HY and demonstrate that this removal does not materially alter the predictions that the model is able to make. This strengthens our belief that the forward-angle diffraction model, even in its simple form, is useful for analyzing direct reactions, particularly when (a) both incident and emergent particles are strongly absorbed and (b) the center of mass of the bound state has a small binding energy. The latter criterion, when added to (a), allows us to justify our assumption that the dominant overlap between the initial and final states occurs outside the nucleus. Thus, what we mean by the criterion that the binding energy of the relevant bound-state wave function be small is that the characteristic falloff distance, α^{-1} [see Eq. (3)] of the center of mass of the captured particles in stripping, for instance, be large compared to the mean free path of the incident or outgoing particle in the nucleus. This is not a strong condition for complex-particle reactions [e.g., (He^3,n),(α,d)], because the relative motion of the capture system generally corresponds to a highly excited center-of-mass bound state in order that the relative motion have appreciable overlap with the internal wave function of the incident particle (e.g., He^3, α, above) for stripping. Nor is it a strong condition if the radial integrand of the reaction matrix happens to be a sharply peaked function, as in the case of inelastic scattering.[3]

We shall first briefly recapitulate the previous assumptions and results.

(a) A sharp boundary is assumed close to the nuclear surface. Strong absorption is taken to occur inside this region of radius R; outside of it distortion effects, other than the shadowing caused by absorption, are neglected. Our chief argument for this approximation (which we shall retain) is that for weakly bound states, most of the contribution to the distorted-wave matrix elements of the form

$$\mathfrak{M}_l = \langle \chi_f^- | \phi_l | \chi_i^+ \rangle \quad (1)$$

* Supported in part by the U. S. Atomic Energy Commission under Contract A. T. (45-1)-1338, program B.

[1] E. M. Henley and D. U. L. Yu, Phys. Rev. **133**, B1445 (1964). This paper is referred to as HY hereafter.

[2] See, for instance, L. D. Landau and Ya. Smorodinsky, *Lectures on Nuclear Theory* (Plenum Press, Inc., New York, 1959), pp. 103–104; D. V. Bugg, A. J. Oxley, J. A. Zoll, J. G. Rushbrooke, V. E. Barnes *et al.*, Phys. Rev. **133**, B1017 (1964); A. Dar, M. Kugler, Y. Dothan, and S. Nussinov, Phys. Rev. Letters **12**, 82 (1964).

[3] J. S. Blair, Phys. Rev. **115**, 928 (1959).

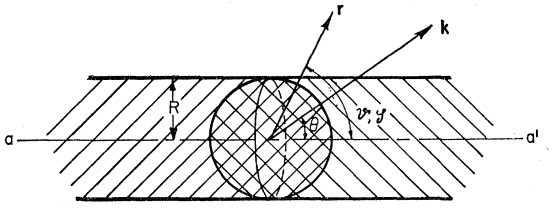

FIG. 1. Pictorial representation of the forward-angle diffraction model. The incident wave propagates from a to a' and the outgoing wave along $\mathbf{k}$. The diffraction radius is R. The incident beam is assumed not to penetrate the region with slanted lines of negative slope, whereas the shadow region for the outgoing particles is taken to be the region of lines with positive slope.

arises from regions outside the nucleus.[4] In Eq. (1), the χ's are the scattering-state wave functions and ϕ_l is the bound state "form factor" characterized by an angular momentum l.[5]

(b) A WKB approximation is made; that is, the incident and emergent waves are assumed to propagate in straight lines and to be plane waves outside the absorption and shadow regions. For the incident wave the shadow is assumed to be a semi-infinite cylindrical region "behind" the sphere of radius R (Fig. 1). It is true that there is a "healing distance" beyond which the beam is refracted and penetrates into the shadow again, but this is assumed to be far enough away that the exponential decrease of ϕ_l in Eq. (1) makes its effects negligible.

(c) Coulomb effects are neglected. This assumption will not influence the cross section significantly as long as the incident energy is well above the Coulomb barrier of the target nucleus.

(d) A forward-angle approximation is made on the geometry of the shadow for the emergent wave; hence, the axis of this shadow is assumed to coincide with that of the incident wave so that the two shadow regions are mirror images of each other about the center of the nucleus (Fig. 1). In effect, there is an infinite cylindrical region which is completely inaccessible to the matrix element of Eq. (1). This assumption brings in a physical asymmetry which destroys time-reversal invariance except for forward scattering. However, this is expected to be unimportant for small scattering angles.

(e) Since only the tail of the center of mass of the bound-state wave function is relevant in the spatial regions of interest, an asymptotic form is assumed for ϕ_l in Eq. (1); it is replaced by the zeroth-order spherical Hankel function $\exp(-\alpha r)/r$ for all values of l. This allows the radial integration to be readily performed.

With the above assumptions the overlap integral (1) can be easily evaluated in the entire space outside the shaded regions in Fig. 1. Diffraction-like structure is exhibited in the cross sections

$$\frac{d\sigma_l}{d\Omega} \propto \sum_{m=-l}^{l} \left| J_m(kR\sin\theta) \times \int_0^\pi d\vartheta \Theta_l^m(\vartheta) \frac{1}{y^2} e^{-Ry\csc\vartheta}(\sin\vartheta + Ry) \right|^2, \quad (2)$$

with $y=\alpha - i(K-k\cos\theta)\cos\vartheta$. In Eq. (2), K and k are, respectively, the incident and outgoing wave numbers, θ is the scattering angle and α is the inverse of the characteristic falloff distance for the bound-state asymptotic wave function ϕ_l; α can be related to a binding energy E by ($\hbar=c=1$)

$$\alpha \simeq (2\mu E)^{1/2}, \quad (3)$$

where μ is the reduced mass (relative to the nucleus) of the particle(s) transferred or excited in the reaction. The Θ_l^m's are directly related to the normalized spherical harmonics by

$$Y_l^m(\vartheta,\phi) = (2\pi)^{-1/2}\Theta_l^m(\vartheta)e^{im\phi}. \quad (4)$$

Equation (2) shows that the angular distribution is characterized by cylindrical Bessel functions of all orders up to l. In the derivation of this result, a further forward-angle approximation is made,

$$|k\sin\vartheta\sin\theta| \ll |y|. \quad (5)$$

This is consistent with assumption (c) and it restricts the validity of this model to angles $\theta \lesssim \sin^{-1}(\alpha/k)$. It is worth noting that, unlike the Butler theory,[6] this model predicts a forward peak for all $l=0$ transitions, independent of the momentum transfer, $q=|\mathbf{K}-\mathbf{k}|$. If the binding energy is sufficiently large (corresponding to a large value of α), the weighting factors for the various m substates peak strongly at $\vartheta=\frac{1}{2}\pi$, and the Fraunhofer nature of Eq. (2) becomes more apparent[3]

$$\frac{d\sigma_l}{d\Omega} \propto \sum_m |J_m(kR\sin\theta)\Theta_l^m(\tfrac{1}{2}\pi)|^2. \quad (6)$$

In this case, only Bessel functions of even *or* odd orders up to l, depending on whether l is even or odd, enter into the cross section because of the properties of the spherical harmonics. Comparisons of the forward-angle model, Eq. (2), with some typical experiments,[7-9] are shown in Figs. 2(a), (b), and (c).

In the following section, we shall further develop the diffraction model, removing some of the approximations inherent in Eq. (2); time reversal symmetry will be restored; a properly normalized asymptotic bound state

[4] In the distorted-wave calculations reported in HY, we found that cutting off the numerical radial integration at $r_0A^{1/3}+d$, where d is the diffuseness of the optical potential, led to but a small change in the matrix element of the $C^{12}(He^3,n)O^{14}$ reaction.

[5] See, for instance, N. Austern, R. M. Drisko, E. C. Halbert, and G. R. Satchler, Phys. Rev. **133**, B3 (1964).

[6] S. T. Butler, Proc. Roy. Soc. (London) **A208**, 559 (1951).

[7] R. Jahr, Phys. Rev. **129**, 320 (1963).

[8] J. B. Ball, C. B. Fulmer, and C. D. Goodman, Phys. Rev. **130**, 2342 (1963).

[9] A. Isoya and M. J. Marrone, Phys. Rev. **128**, 800 (1962).

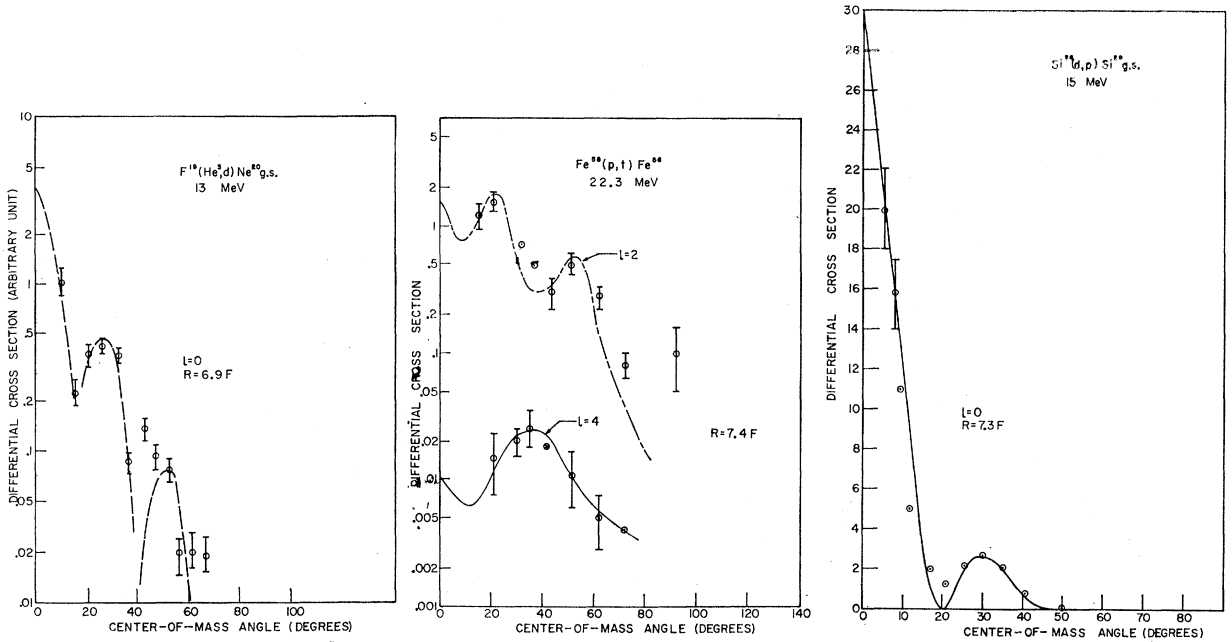

(a) (b) (c)

FIG. 2. Three examples of the fit of Eq. (2) to experiments are shown: (a) ground-state transition for the $F^{19}(He^3,d)Ne^{20}$ reaction (Ref. 7), (b) the $Fe^{58}(p,t)Fe^{56}$ reaction for $l=2$ and 4 (Ref. 8); both curves are fitted with the same value of R, and (c) ground-state transition for the $Si^{28}(d,p)Si^{29}$ reaction (Ref. 9).

wave function will be used; a brief discussion of Coulomb effects will also be given.

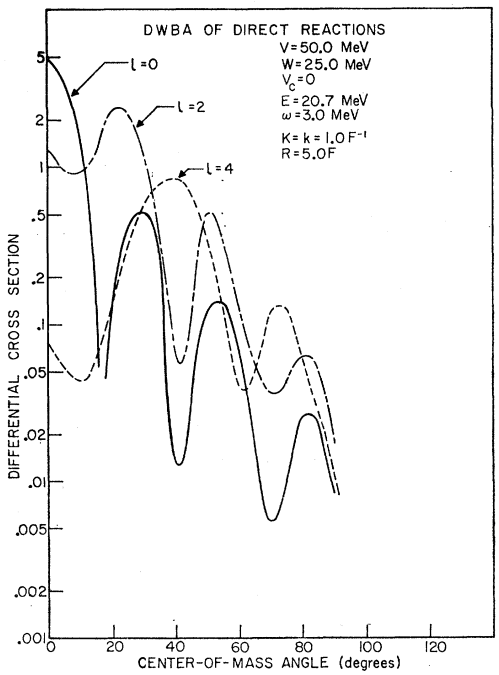

FIG. 3. Typical distorted-wave Born approximation calculations of direct nuclear reactions without Coulomb interaction. V and W are the real and imaginary parts of the Saxon potential, ω is the energy spacing of a harmonic oscillator. Transitions for $l=0$, 2, and 4 are shown.

II. FURTHER DEVELOPMENTS

For charged projectiles, although we can, in principle, employ Coulomb waves for the scattering states and test their effects in terms of the diffraction model, it turns out to be simpler to appeal to distorted-wave calculations.[1] In Fig. 3 we show the results of a typical calculation for a stripping or pickup reaction; angular distributions for $l=0$, 2, and 4 are plotted; parameters for the optical potential also appear. In Fig. 4 we show the differential cross section that results when a Coulomb potential of barrier height $\approx 40\%$ of the incident energy is added. Comparison of Figs. 3 and 4 confirms that the Coulomb effects on the differential cross sections are only secondary: Angular widths are slightly increased and magnitudes of cross sections somewhat depressed; these effects are expected on physical grounds. Morinigo[10] has also estimated the Coulomb effects for stripping reactions with zero angular momentum transfer in Born approximation and found that only the magnitude of the cross section is slightly altered. For heavy elements, when the Coulomb barrier becomes comparable to the incident energy, some of these remarks concerning the neglect of the Coulomb effects lose their validity. However, for most cases for which the diffraction model is sensible, we feel that this neglect is justified and shall not, therefore, consider its effects further.

As remarked earlier, the forward-angle approximation

[10] F. B. Morinigo, Phys. Rev. 133, B65 (1964).

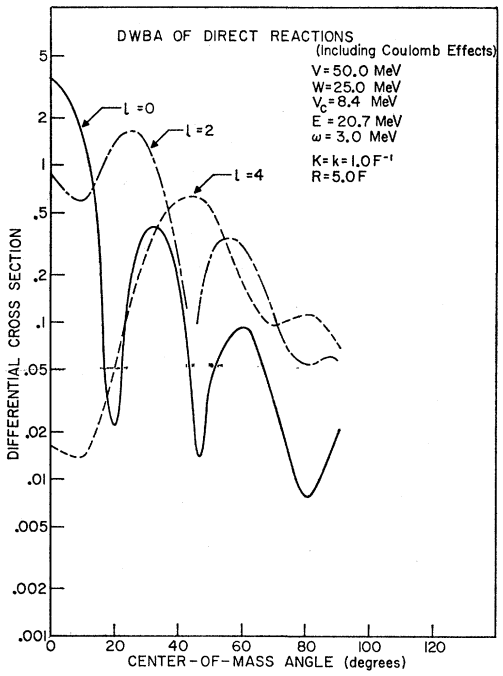

FIG. 4. The same distorted-wave Born approximation calculations as those of Fig. 3, but with identical Coulomb interactions in the incident and exit channels.

on the shadow geometry introduces an asymmetry between the incident and outgoing wave vectors, **K** and **k**; as a result, Eq. (2) shows that the requirement of time-reversal symmetry of the cross section is not satisfied except for $\theta=0°$. Furthermore, the range of applicability of the model is limited to small scattering angles. We shall presently remove this approximation and show that its effect is small. Thus we consider the axes of the cylindrical shadows to lie parallel to their respective wave vectors. The geometry of the shadows becomes, instead of one infinite cylinder, *two* semi-infinite cylinders tangent to the absorbing sphere. This is shown in Fig. 5(a). The angle between the axes of these shadows decreases as the scattering angle increases.

In order to carry out the overlap integral (1) over the entire region outside the shadows, it is convenient to divide the open space into four subregions A, B, C, and D, also shown in Fig. 5(a). The boundaries, represented by dotted lines, are infinite planes perpendicular to the figure. The shadow geometry is completely symmetric about the $\vartheta=0$, $\phi=0$ plane (labeled 0 in Fig. 5). This naturally restores the time-reversal symmetry since the cross section is invariant on interchanging the incident and emergent wave vectors and reversing their directions. The bound-state wave functions ϕ_l should be the lth order spherical Hankel functions outside the range of the nuclear potential. However, for simplicity, we will temporarily continue to use their asymptotic form in order to investigate the effects due solely to the forward-angle approximation. (Properly normalized external wave functions will be employed later.) Hence the limits of integration for the four subregions can be written as follows:

$$\mathfrak{M}_l{}^m=\int_\tau e^{-i\mathbf{k}\cdot\mathbf{r}}e^{-\alpha r}Y_l{}^{m*}(\vartheta,\phi)e^{i\mathbf{K}\cdot\mathbf{r}}r dr\sin\vartheta d\vartheta d\phi\,, \quad (7)$$

with

$$\int_\tau=\int_\phi\int_\vartheta\int_r=\iiint_A+\iiint_B+\iiint_C+\iiint_D$$

$$=\int_0^\pi\int_0^{\delta_a}\int_{R_a}^\infty+\int_\pi^{2\pi}\int_0^{\delta_b}\int_{R_b}^\infty$$

$$+\int_0^\pi\int_{\delta_a}^\pi\int_R^\infty+\int_\pi^{2\pi}\int_{\delta_b}^\pi\int_R^\infty\,, \quad (8)$$

where R_a and R_b are determined by the surfaces of the semi-infinite cylinders in A and B, which can be expressed by the equations of constraint $R_i\sin\gamma_i=R$ (with $i=a$ or b). γ_a and γ_b are the angles which the radius vector **r** makes, respectively, with the axes of the

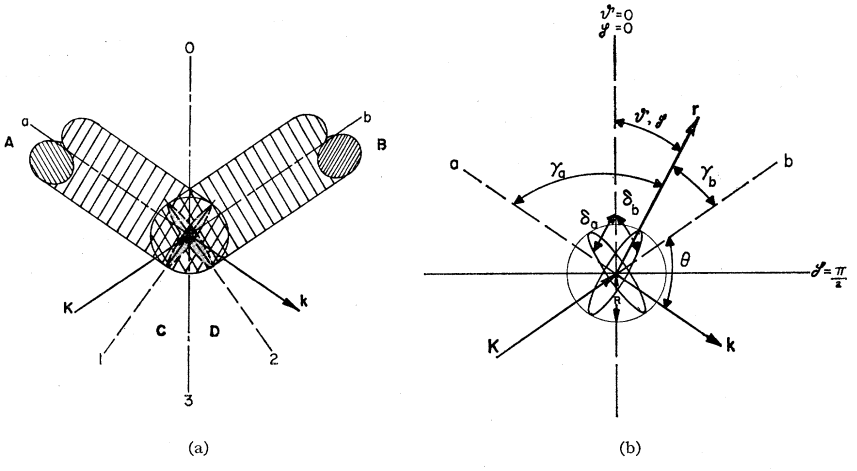

FIG. 5. Pictorial representation of the large-angle diffraction model. The shadow geometry is shown in (a) and the relevant vectors and angles are defined in (b).

cylinders in A and B, and can be related to the scattering angle by well-known trigonometric relations:

$$\cos\gamma_{a,b}=\cos\vartheta\,\sin(\tfrac{1}{2}\theta)\mp\sin\vartheta\,\cos(\tfrac{1}{2}\theta)\sin\phi, \tag{9}$$

where $-$ goes with a and $+$ with b. The boundary planes between the regional pairs A, C, and B, D, [labeled (1) and (2), respectively, in Fig. 5] are also perpendicular to the cylinders a and b. The angles δ_a and δ_b in Eq. (8) characterize the geodesics at the intersections of these boundary planes and the absorbing sphere. They can also be related to the scattering angles,

$$\cot\delta_{a,b}=\mp\cot(\tfrac{1}{2}\theta)\sin\phi, \tag{10}$$

with the sign as in Eq. (9). Putting

$$\mathbf{k}\cdot\mathbf{r}=-kr\cos\gamma_a,$$
$$\mathbf{K}\cdot\mathbf{r}=Kr\cos\gamma_b, \tag{11}$$

and substituting Eqs. (4), (9), (10), and (11) into Eqs. (7) and (8), we have

$$\mathfrak{M}_l{}^m=\int_\tau e^{-(p-\mathfrak{q}\sin\phi)r}(2\pi)^{-1/2}\Theta_l{}^{m*}(\vartheta)e^{-im\phi}r\,dr\,\sin\vartheta\,d\vartheta\,d\phi, \tag{12}$$

with

$$p=\alpha-i(K+k)\cos\vartheta\,\sin\tfrac{1}{2}\theta,$$
$$\mathfrak{q}=i(K-k)\sin\vartheta\,\cos\tfrac{1}{2}\theta. \tag{13}$$

The radial integrals can be readily carried out and we obtain

$$\begin{aligned}\mathfrak{M}_l{}^m=&\int_0^{\pi}\int_0^{\delta_a}\left(\frac{1}{p-\mathfrak{q}\sin\phi}+\frac{R}{\sin\gamma_a}\right)\frac{\exp[-(p-\mathfrak{q}\sin\phi)R\csc\gamma_a]}{p-\mathfrak{q}\sin\phi}Y_l{}^{m*}(\Omega)d\Omega\\&+\int_0^{\pi}\int_{\delta_a}^{\pi}\left(\frac{1}{p-\mathfrak{q}\sin\phi}+R\right)\frac{\exp[-(p-\mathfrak{q}\sin\phi)R]}{p-\mathfrak{q}\sin\phi}Y_l{}^{m*}(\Omega)d\Omega\\&+\int_{\pi}^{2\pi}\int_0^{\delta_b}\left(\frac{1}{p-\mathfrak{q}\sin\phi}+\frac{R}{\sin\gamma_b}\right)\frac{\exp[-(p-\mathfrak{q}\sin\phi)R\csc\gamma_b]}{p-\mathfrak{q}\sin\phi}Y_l{}^{m*}(\Omega)d\Omega\\&+\int_{\pi}^{2\pi}\int_{\delta_b}^{\pi}\left(\frac{1}{p-\mathfrak{q}\sin\phi}+R\right)\frac{\exp[-(p-\mathfrak{q}\sin\phi)]}{p-\mathfrak{q}\sin\phi}Y_l{}^{m*}(\Omega)d\Omega.\end{aligned} \tag{14}$$

Because of the geometrical symmetry, the integrands for the subregions B, D can be absorbed into those for subregions A, C by a change of variable

$$\phi\rightarrow\phi+\pi. \tag{15}$$

Under this transformation,

$$\delta_b\rightarrow\delta_a,\quad R_b\rightarrow R_a. \tag{16}$$

Thus, the overlap integral becomes

$$\begin{aligned}\mathfrak{M}_l{}^m=&\int_0^{\pi}(2\pi)^{-\frac{1}{2}}e^{-im\phi}d\phi\left\{\int_0^{\delta_a}d\vartheta e^{-pR\csc\gamma_a}\Theta_l{}^{m*}(\vartheta)\sin\vartheta\left[\left(\frac{1}{p-\mathfrak{q}\sin\phi}+\frac{R}{\sin\gamma_a}\right)\frac{\exp[\mathfrak{q}R\sin\phi\csc\gamma_a]}{p-\mathfrak{q}\sin\phi}\right.\right.\\&\left.+(-1)^m\left(\frac{1}{p+\mathfrak{q}\sin\phi}+\frac{R}{\sin\gamma_a}\right)\frac{\exp[-\mathfrak{q}R\sin\phi\csc\gamma_a]}{p+\mathfrak{q}\sin\phi}\right]+\int_{\delta_a}^{\pi}d\vartheta e^{-pR}\Theta_l{}^{m*}(\vartheta)\sin\vartheta\\&\left.\times\left[\left(\frac{1}{p-\mathfrak{q}\sin\phi}+R\right)\frac{\exp(\mathfrak{q}R\sin\phi)}{p-\mathfrak{q}\sin\phi}+(-1)^m\left(\frac{1}{p+\mathfrak{q}\sin\phi}+R\right)\frac{\exp(-\mathfrak{q}R\sin\phi)}{p+\mathfrak{q}\sin\phi}\right]\right\}.\end{aligned} \tag{17}$$

The double integral is evaluated numerically on an IBM-709 computer. Results are shown in Figs. 6–10. Differential cross sections for $l=0$, 2, and 4 transitions are compared with those of Eq. (2). It is seen that for most transitions Eq. (2) is a good approximation to the angular distribution predicted by Eq. (17) at least up to $\theta=40°$. We have also looked at the effect of only removing from Eq. (2) the approximation shown in Eq. (5) and found that the cross sections become even more closely akin to those that follow from Eq. (17). They are also plotted in Figs. 6–10 for comparison. For odd-l states, Eq. (17) continues to predict a minimum in the cross section at 0°, as Eq. (2) did before.

The above development thus generalizes in a natural manner the diffraction model introduced earlier. However, much of the simplicity, other than *Anschaulichkeit*, has been lost, since a double numerical integration is required. The unique advantage over the forward-angle approximation of the model, is that it can be used for a wider region of angles. It agrees, as it should, with the

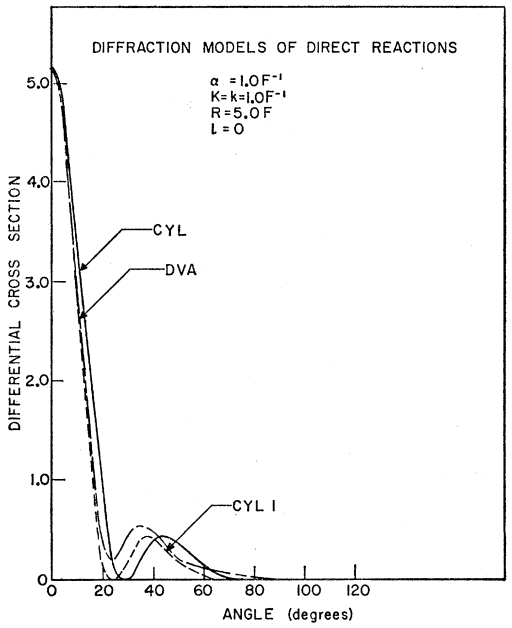

FIG. 6. Prediction of the generalized diffraction model (labeled DVA), Eq. (17), for $l=0$ with $K=k=1.0$ F^{-1} and $R=5$ F. This is compared with the forward-angle approximation (CYL), Eq. (2). The effect of removing the approximation of Eq. (5) is also shown (CYL1).

forward-angle model for not too large angles ($\theta \lesssim 40°$).

There are, however, other simpler ways in which time reversal can be preserved. One such method has recently been discussed by Dar.[11] It amounts to replacing $kR\sin\theta$ in the forward-angle approximation of our Eq. (2) by qR, where $q=|\mathbf{K}-\mathbf{k}|$. This *ad hoc* assumption is not justified by him, and it leads to a different prediction from ours for small angles which can be tested experimentally. Thus, Dar's treatment, unlike ours, does not necessarily give 0° peaking for all $l=0$ transitions for which the model is applicable. It is true that a radius can be chosen such that $J_0(qR)$ has a maximum at 0°. However, a variation of the experimental energy, for a given target, shifts the maximum of $J_0(qR)$ to other angles (this assumes, of course, that R is energy-independent).

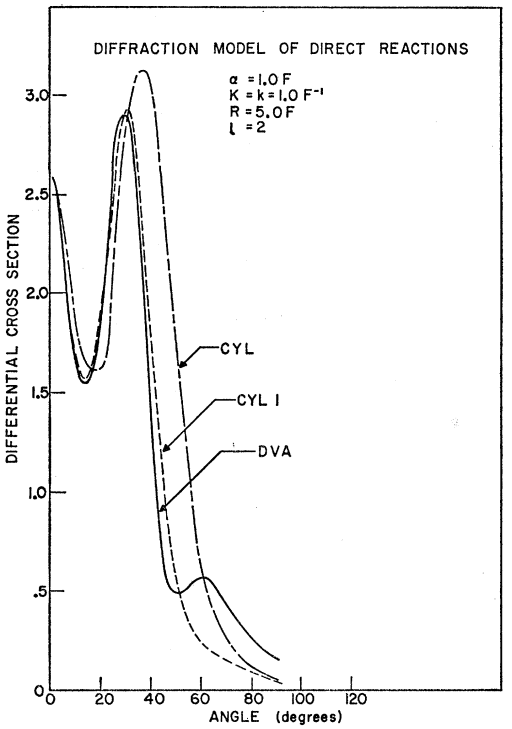

FIG. 7. Same as Fig. 6, but for $l=2$.

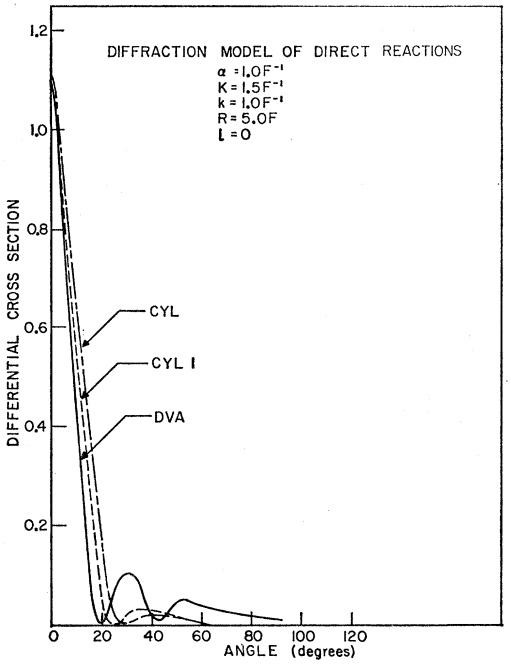

FIG. 8. Prediction of the generalized diffraction model (labeled DVA), Eq. (17), for $l=0$ with $K=1.5$ F^{-1}, $k=1.0$ F^{-1} and $R=5$ F. This is compared with the forward angle approximation (CYL), Eq. (2). The effect of removing the approximation of Eq. (5) is also shown (CYL1).

We shall illustrate two simple methods of generalizing the forward-angle diffraction model, which preserve time-reversal invariance, and at the same time retain the forward peaking which appears to be observed experimentally[12] (Fig. 2) in medium-energy reactions of the type we are discussing. Akin to an approximation suggested by Glauber,[13] we consider the axis aa' of the single infinitely long cylindrical shadow of Fig. 1 to lie along the vector $\mathbf{K}+\mathbf{k}$, whose magnitude is invariant under time reversal. This algebraic symmetry restores

[11] A. Dar, Phys. Letters **7**, 339 (1963).

[12] See, for instance, J. H. Manley, Phys. Rev. **130**, 1475 (1963) and Refs. 7–9.

[13] R. J. Glauber, in *Lectures on Theoretical Physics*, edited by W. E. Brittin, B. W. Downs, and J. Downs (Interscience Publishers, Inc., New York, 1959), Vol. I, p. 345.

TR invariance to the computed matrix element, which then takes the form

$$\mathfrak{M}_l^m=(2\pi)^{1/2}\int_0^\pi d\vartheta J_m(qR\sin\gamma\sin\vartheta)\Theta_l^m(\vartheta)\times\exp(-tR\csc\vartheta)(\sin\vartheta+tR)/t^2, \quad (18)$$

with

$$\sin\gamma=\left\{1-\frac{1}{q^2}\left[\frac{(K/k)+\cos\theta}{[(\sin\theta/K)^2+(1/k+\cos\theta/K)^2]^{1/2}}-\frac{(k/K)+\cos\theta}{[(\sin\theta/k)^2+(1/K+\cos\theta/k)^2]^{1/2}}\right]^2\right\}^{1/2}, \quad (19)$$

and

$$t=\alpha-iq\cos\gamma\cos\vartheta. \quad (20)$$

Note that $\sin\gamma$ vanishes at $\theta=0°$ so that for $l=0$ there is always a forward peak independent of momentum transfer q. Again, if α is large, Eq. (18) leads to

$$\frac{d\sigma}{d\Omega}\propto\sum_{m=-l}^{l}|J_m(qR\sin\gamma)\Theta_l^m(\tfrac{1}{2}\pi)|^2. \quad (21)$$

Thus, our direct generalization, Eq. (18), of Eqs. (2) and (6) suggests that an approximate way to incorporate time-reversal invariance is to replace the factor $k\sin\theta$ in the argument of the Bessel function by $q\sin\gamma$, and not by q alone, as one might at first sight assume.[11] In deriving Eq. (18), a forward-angle approximation

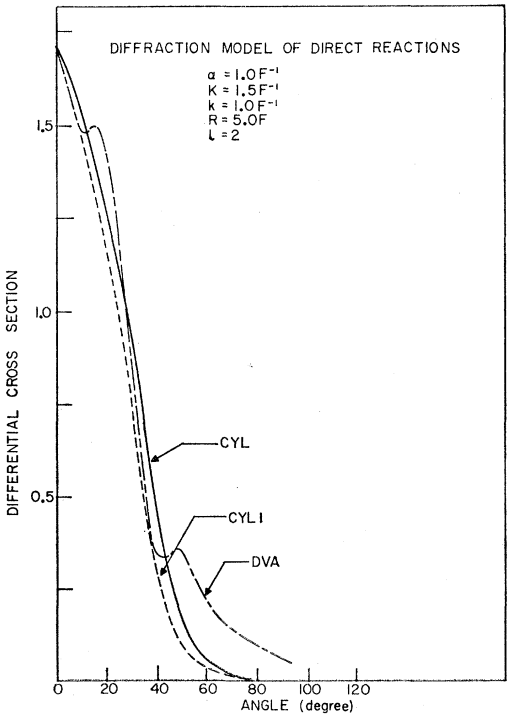

FIG. 9. Same as Fig. 8, but for $l=2$.

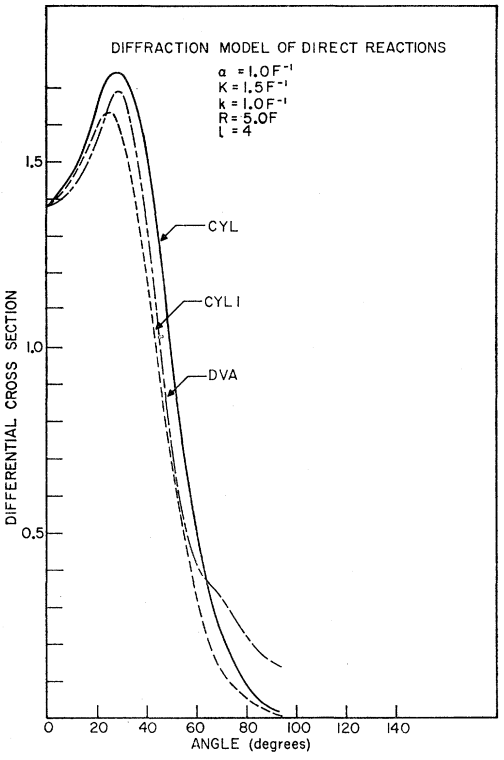

FIG. 10. Same as Fig. 8, but for $l=4$.

similar to Eq. (5) has been retained

$$|q\sin\gamma\sin\vartheta|\ll|t|. \quad (22)$$

The above choice is not unique. Thus, TR invariance can also be restored by other choices of geometrical symmetry for the shadow regions. We can, for instance, consider the axis of the infinite cylindrical shadow to lie along the bisector of the scattering angle, that is, half-way between the wave vectors $\mathbf{k}$ and $\mathbf{K}$. The expressions for the cross sections are the same as those in Eqs. (18) and (20)–(22) while Eq. (19) is replaced in this case by

$$\sin\gamma=[1-(1/q^2)(K-k)^2\cos^2\tfrac{1}{2}\theta]^{1/2}. \quad (23)$$

We note again that $\gamma=0$ when $\theta=0$.

In the special case when $K=k$, the two ways of restoring time reversal give the same results. Also in this case the matrix element of Eq. (18) may be further simplified; thus,

$$\mathfrak{M}_l^m=(2\pi)^{1/2}\int_0^\pi d\vartheta J_m(qR\sin\vartheta)\Theta_l^m(\vartheta)\times e^{-\alpha R\csc\vartheta}(\sin\vartheta+\alpha R)/\alpha^2. \quad (24)$$

Due to the factor $\exp(-\alpha R\csc\vartheta)$, the integrand is strongly peaked at $\vartheta=\frac{1}{2}\pi$, and we can write

$$\mathfrak{M}_l^m\simeq(2\pi)^{1/2}J_m(qR)\Theta_l^m(\tfrac{1}{2}\pi)(1+\alpha R)I_0/\alpha^2, \quad (25)$$

where I_0 is a number,

$$I_0=\int_0^\pi e^{-\alpha R\csc\vartheta}d\vartheta\simeq\pi\exp(-3\alpha R/2)J_0(i\alpha R/4). \quad (26)$$

The corresponding cross section is

$$\frac{d\sigma_l}{d\Omega} \propto \sum_{m=-l}^{l} |J_m(2kR \sin\tfrac{1}{2}\theta)\Theta_l^m(\tfrac{1}{2}\pi)|^2. \quad (27)$$

This differs from Eq. (6) in that the argument of the Bessel function is $2kR \sin\frac{1}{2}\theta$ instead of $kR \sin\theta$;[14] it has the effect of sharpening the angular width of the differential cross section, as the zeroth-order Bessel function reaches its minimum faster. In addition to time-reversal invariance and the 0° peaking in the cross section, Eqs. (18), (21), and (27) also give closer agreement to the shapes of the forward peaks predicted by the generalized diffraction model depicted in Fig. 5. Although the range of applicability of these equations is still limited to small scattering angles because of an assumption made in Eq. (22), this can be easily remedied.

Finally, the asymptotic bound-state wave functions outside the range of the potential are the lth (not only zeroth) order spherical Hankel functions of the first kind, h_l, which satisfy the recursion relation

$$h_{l-1}(\rho)+h_{l+1}(\rho)=[(2l+1)/\rho]h_l(\rho), \quad l>0, \quad (28)$$

with

$$h_l(\rho)=-i(-1)^l\rho^l(d/\rho d\rho)^l(e^{i\rho}/\rho), \quad (29)$$

and $\rho=i\alpha r$. $h_l(\rho)$ is purely real or imaginary depending on whether l is even or odd. We match this exterior solution onto the interior radial nuclear wave function.

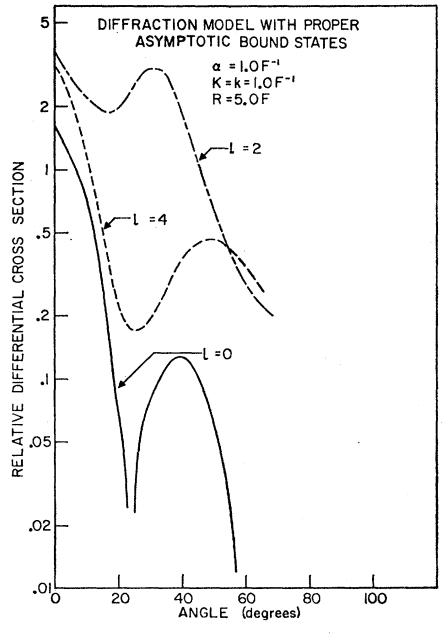

FIG. 11. Differential cross sections predicted by the diffraction model with spherical Hankel functions for ϕ_l are plotted for $l=0$, 2, and 4 with $K=k=1.0$ F^{-1} and $R=5$ F.

[14] Note that this says that *only* when $K=k$ can $kR \sin\theta$ be replaced by qR at small angles for the argument of the Bessel function.

For a direct single-particle excitation or transfer reaction, the inside wave function can be represented by an eigenfunction of a finite Saxon-type potential. For many-particle excitation or transfer reactions, it is more convenient to assume a shell-model infinite harmonic-oscillator representation $\Re_{nl}(r)$ for the interior bound-state wave function. The advantage of this choice is that the parts involving respectively the center of mass and the relative coordinates can be easily separated; only the center-of-mass part enters into Eq. (1).[1] In this case normalization is completed in two steps:

(a) We require continuity of the logarithmic derivative of the exterior and interior wave functions at the radius R, i.e. (we suppress the principal quantum number, n, of $\Re_{nl}$)

$$[(\partial/\partial r)h_l(i\alpha r)]/h_l(i\alpha r)|_{r=R} = [(\partial/\partial r)\Re_l(r)]/\Re_l(r)|_{r=R}. \quad (30)$$

This condition relates α to ω, the oscillator energy-level spacing.

(b) The entire wave function must be normalized, i.e.,

$$\int_0^R |\Re_l(r)|^2 r^2 dr + \left|\frac{\Re_l(R)}{h_l(i\alpha R)}\right|^2 \times \int_R^\infty |h_l(i\alpha r)|^2 r^2 dr = \frac{1}{|A_l|^2}. \quad (31)$$

This condition determines the modulus of the normalization constant A_l. Thus, the bound-state wave function in Eq. (1) is

$$\phi_l(\mathbf{r}) = A_l \Re_l(r) Y_l^m(\vartheta,\phi), \quad r \leqslant R,$$
$$= A_l^* \frac{\Re_l(R)}{h_l^*(i\alpha R)} h_l(i\alpha r) Y_l^m(\vartheta,\phi), \quad r \geqslant R. \quad (32)$$

In an evaluation of the overlap integral only the external part ($r \geqslant R$) of Eq. (32) is relevant.

We have shown previously that the forward-angle approximation of the shadow geometry does not significantly influence the magnitude and shape of the angular distribution at small scattering angles. Thus, for this purpose, we continue to use the same shadow geometry as in Fig. 1, as this considerably simplifies the calculation.

With plane waves for the scattering states outside the shadow region, the overlap integral becomes

$$\mathfrak{M}_l^m = (2\pi)^{-1/2} A_l^* \frac{\Re_l(R)}{h_l^*(i\alpha R)} \int_0^{2\pi} \int_0^{\pi} \int_{R\csc\vartheta}^{\infty} \exp\{ir[(K-k\cos\theta)\cos\vartheta - k\sin\theta\sin\vartheta\cos\phi]\} \times h_l^*(i\alpha r)\Theta_l^{m*}(\vartheta) e^{-im\phi} r^2 dr \sin\vartheta d\vartheta d\phi. \quad (33)$$

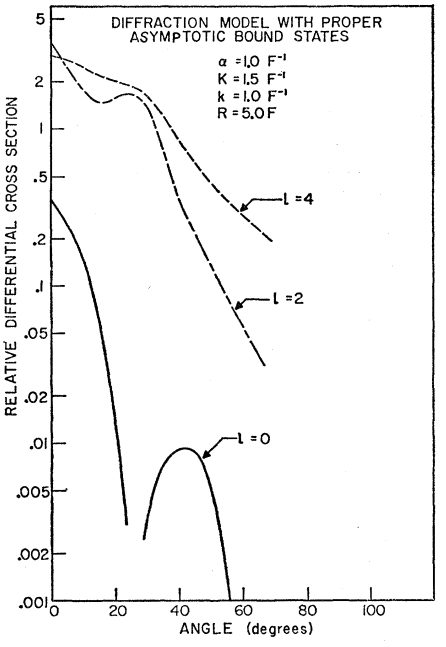

FIG. 12. Same as Fig. 11 except $K=1.5$ F^{-1}, $k=1.0$ F^{-1}.

After performing an integration over the azimuthal angles ϕ, we have

$$\mathfrak{M}_l{}^m=(2\pi)^{+1/2}A_l{}^*\frac{\mathfrak{R}_l(R)}{h_l{}^*(i\alpha R)}\int_0^\pi \Theta_l{}^{m*}(\vartheta)\sin\vartheta d\vartheta$$

$$\times\int_{R\csc\vartheta}^\infty J_m(Qr)h_l{}^*(i\alpha r)\exp(i\mathfrak{\lambda}\cdot\mathbf{r})r^2dr\,, \quad (34)$$

where $Q=k\sin\theta\sin\vartheta$, and $\mathfrak{\lambda}=\mathbf{K}(1-k/K\cos\theta)$. In order to restore time reversibility in Eq. (34), one merely has to replace Q by $q\sin\gamma\sin\vartheta$, where $\sin\gamma$ is given by Eq. (19) or by Eq. (23).

Without further approximation, it does not appear that the double integral in Eq. (34) can be carried out analytically. However, a straightforward numerical integration on the IBM-709 can be used for its evaluation.[15] Results for $l=0$, 2 and 4 are shown in Fig. 11 for $K=k=1$ F^{-1}. As the difference between the two wave numbers increases, there is indication that enhancement to higher l transitions is predicted. This is brought out in Fig. 12, where $K=1.5$ F^{-1} and $k=1$ F^{-1}. It should be noted, however, that this normalization procedure also changes the shapes of angular distributions when compared with the previous models. In particular, transitions for high l's have broader forward peaks. This arises from the fact that higher order spherical Hankel functions fall off more slowly than the zeroth-order one and this has the effect of decreasing the value of α in Eq. (2) for these transitions.

III. CONCLUSIONS

The generalizations which we have made on a simple diffraction model for direct reactions, presented earlier,[1] show that the major conclusions based on the simple model persist. An example is the forward peak predicted for all zero-angular momentum transfer ($l=0$) reactions, independent of linear momentum transfer. We have argued that Coulomb effects are only secondary if the barrier height is below and not too close to the incident energy. Among the generalizations considered, the removal of the forward-angle approximation does not significantly change the predicted angular distributions. On the other hand, the use of spherical Hankel functions, rather than their asymptotic form, as bound-state wave functions broadens the angular distributions somewhat for higher l transitions. However, the use of correct external wave functions allows absolute cross sections to be computed. The observation that higher l transitions are enhanced as $|K-k|$ increases follows from this generalized model, as it did for the simpler model.[1]

More work on the diffraction model will be directed toward a better understanding of *why* the model works as well as it does. In particular, assumptions (a) and (b) listed in Sec. I require further justification.

[15] The main disadvantage is that, since the integrands are highly oscillatory, a fine mesh is necessary and, consequently, a large amount of machine time is required for the integration.